Electrochemical detection of homovanillic acid, a breast cancer biomarker, using Pluronic-modified MoS_2 nanosheets

Zniber, Mohammed; Vahdatiyekta, Parastoo; Roy, Shounak; Nikiforow, Kostiantyn; Jaiswal, Amit; Huynh, Tan-Phat

Published in:
Nano Futures

DOI:
10.1088/2399-1984/ac8215

Published: 26/08/2022

Document Version
Accepted author manuscript

Document License
CC BY-NC-ND

Electrochemical detection of homovanillic acid – a breast cancer biomarker using Pluronic-modified MoS_2 nanosheets

Mohammed Zniber[1], Parastoo Vahdatiyekta[1], Shounak Roy[2], Kostiantyn Nikiforow[3], Amit Jaiswal[2,*], Tan-Phat Huynh[1,*]

[1] *Laboratory of Molecular Sciences and Engineering, Åbo Akademi University 20500 Turku, Finland*

[2] *School of Basic Sciences, Indian Institute of Technology Mandi, Kamand, Mandi 175005, Himachal Pradesh, India*

[3] *Institute of Physical Chemistry, Polish Academy of Sciences, 44/52 Kasprzaka, 01-224 Warsaw, Poland*

E-mail address: j.amit@iitmandi.ac.in; tan.huynh@abo.fi

Abstract: Two-dimensional transition metal dichalcogenides (2D TMDs) have gained considerable attention from the scientific community for their various applications thanks to their remarkable chemical, physical, optical and electronic properties. In this study, MoS_2 nanosheets were synthesized using a kitchen blender with the assistance of a surfactant so-called Pluronic F127 through a shear-exfoliation process. Different techniques were used to characterize the chemical composition, nanostructure, and electrochemical properties of the synthesized MoS_2-F127 as well as Pt modified with MoS_2-F127 (Pt/MoS_2-F127) electrode. The Pt/MoS_2-F127 electrode combined with differential pulse voltammetry was used for the electrochemical detection of homovanillic acid (HVA) in the presence of common interferents in urine. The study provides a new approach to discriminate the electrochemical signal of HVA and UA which lead to higher selectivity of the sensor.

1. Introduction

2D transition metal dichalcogenides (TMDs) is a widely used group of materials in biosensing applications. This is due to their many benefits, which make them promising for the development of numerous sensing platforms. MoS_2 is the most popular and highly studied compound of 2D TMDs [1]. MoS_2 exhibits remarkable characteristics, such as mechanical strength, flexibility, and catalytic activity [2,3]. It has been studied in diagnosing metabolic diseases; for instance, functional hybrids of Ni-doped MoS_2 and reduced graphene oxide (rGO) were used in the electrochemical detection of blood glucose in diabetes mellitus. The sensor

demonstrated high electrochemical activity due to its highly displayed catalytic sites, good electron transport rates, high effective surface area, and electrical conduction of rGO and MoS_2 [4]. Similarly, a novel composite consisting of 3D MoS_2 nanoflowers and Cu_2O metal oxide was employed in the non-enzymatic amperometric detection of glucose in alkaline medium. The electrode exhibited an excellent electrochemical activity as a result of the unique structural properties of MoS_2-Cu_2O [5]. Additionally, MoS_2 was also used in the enzymatic detection of glucose. An enzymatic bio-composite based on MoS_2 nanosheets, gold nanoparticles (AuNPs), and glucose oxidase (GOx) modified Au electrodes showed a high sensitivity for glucose because of its 3D structure with large interlayer distance and surface area for enzyme immobilization [6]. MoS_2 based sensors were not only used in the detection of glucose but also for other important biomolecules. Blood cholesterol was also investigated using an electrode containing cholesterol oxidase (Chox), AuNPs, and MoS_2 as it is highly recommended in the diagnosis of atherosclerosis, thrombosis, and cardiovascular diseases [7]. Dopamine was also examined using a combination of MoS_2 nanoflowers, carbon nanotubes, and graphene, which demonstrated an excellent electroactivity for the detection of dopamine [8]. 2D MoS_2 flakes modified with a thiolated DNA probe, was used as an optical biosensor for miRNA21 thanks to the photoluminescence of MoS_2. The results demonstrated high sensitivity and selectivity and showed a future potential for the development of commercial devices [9]. Strong synergistic effect between MoS_2, AuNPs, and rGO was employed in the development of an ultrasensitive electrochemical immunosensor based on MoS_2/AuNPs/rGO nanocomposite to detect CA 27-29 breast cancer antigen with low detection limit (LoD) of 0.08 $U.mL^{-1}$ [10]. An ultrasensitive, low-cost, portable and miniaturized immunosensor based on MoS_2/PDDA hybrid film was prepared using layer-by-layer self-assembly technique. This sensor was employed in the detection of alpha-fetoprotein (AFP). This approach exhibited a linear range from 0.1 ng/mL to 10 ng/mL and a low LoD of 0.033 ng/mL. Moreover, the immunochip was used to detect AFP in human serum samples. It also proved high selectivity when analyzing small volumes, which could be useful in the trace detection of AFP [11]. An electrochemical aptasensor was built using hierarchical MoS_2 nanostructure functionalized with SiO_2 nanoprobes and capped with DNA probe. The sensor was used for the simultaneous detection of prostate specific antigen (PSA) and sarcosine in serum samples [12]. A field effect transistor (FET) sensor array based on MoS_2 nanosheets, was utilized to detect nuclear matrix protein 22 (NMP22) and cytokeratin 8 (CK8) which are known as bladder cancer biomarkers. Thanks to the electronic properties of MoS_2, the proposed sensor showed high sensitivity with LoD as low as 0.027 and 0.019 aM for NMP22 and CK8, respectively [13].

The aforementioned applications of MoS_2-based sensors in cancer diagnosis are highly demanded, as cancer is a major public health problem and leading cause of death worldwide, accounting for 10 million deaths in 2020. The most widespread cancer types in 2020 in terms of new cancer cases are breast, lung, colon and rectum, prostate, skin and stomach cancer, respectively [14]. Cancer encompasses a wide range of diseases involving anomalous cell growth.[15] These processes might produce or cause changes in concentration of biological molecules known as biomarkers, that may be utilized to detect cancer as well as its stage, subtype, and response to therapy [16]. Many of these of biomarkers include peptides, proteins (e.g., an enzyme or receptor), nucleic acids (e.g., a microRNA or other non-coding RNA), antibodies, and other small molecules secreted in urine [17]. Among these, homovanillic acid (HVA) or 4-hydroxy-3-methoxyphenylacetic acid, an important catecholamine metabolite produced by a successive action of monoamine oxidase and Catechol-O-methyltransferase on dopamine [18]. HVA is present in different biospecimens, such as blood, urine, cerebrospinal fluid (CSF), feces, and saliva. HVA has been found to be associated with different diseases, including breast cancer as well as narcolepsy, schizophrenia, celiac disease, sepiapterin reductase deficiency, and phenylketonuria [19–22]. Moreover, HVA, 4-hydroxyphenylacetate, 5-hydroxysindoleacetate, 5-hydroxymethyl-2-deoxyuridine, and 8-hydroxy-2-deoxyguanosine were found in the urine of breast cancer patients and not in healthy individuals [23], indicating their potential use as breast cancer biomarkers.

Various analytical techniques were employed in identifying and quantifying potential biomarkers in urine, such as LC-MS (Liquid Chromatography – Mass Spectrometry), GC-MS (Gas Chromatography – Mass Spectrometry), and NMR (Nuclear Magnetic Resonance) spectroscopy, as well as IELC (Ion Exchange Liquid Chromatography) and IMS (Ion Mobility Spectrometry) [24]. However, they require expensive instrumentation, complex sample pre-treatment, and well-qualified technicians. Hence, alternative approaches are needed for low-cost and simple detection and quantification of biomarkers. Electrochemical-based sensors for detecting particular compounds have captivated a lot of attention over recent years because of their high sensitivity, selectivity, simple preparation, and rapid response [25]. Electrochemical sensors function based on a variety of methods such as amperometry, potentiometry, voltammetry, and electrochemical impedance. A wide variety of materials can be used to make such sensors, including quantum dots, conducting polymers, metal oxides, and composites [26]. As a result, several electrochemical sensors were developed to detect HVA, for instance, a novel electrochemical sensor combining multi-walled carbon nanotubes and platinum

nanoparticles (MWCNTs-PtNPs) for simultaneous determination of HVA and vanillylmandelic acid (VMA) in urine [27]. The sensor demonstrated a good linear response between 0.2 – 80 μM with LoD of 0.008 μM for HVA and 0.173 μM for VMA. Also, HVA was detected alongside vanillylmandelic acid and 5-hydroxyindole-3-acetic acid on screen-printed carbon electrodes using flow injection analysis coupled with amperometric detection. The sensor exhibited a linear range between 0.05 – 100 μM for HVA, VMA, and 5-HIAA with LoD of 0.065 μM, 0.053 μM, and 0.033 μM, respectively [28]. HVA was also detected in urine by a novel electrochemical sensor based on carbon paste electrodes modified with zinc ferrite nanostructure combined with multi-walled carbon nanotubes (ZFO/MWCNTs). The modified sensor demonstrated excellent electrocatalytic activity towards electrochemical oxidation of HVA and good selectivity in the presence of other species like uric acid and dopamine [29]. Differential pulse voltammetry (DPV) combined with hollow fiber – based liquid-phase microextraction (HF-LPME) was used for the determination of HVA in urine. This method showed increased selectivity as well as a low LoD and quantification achieved by LPME [30]. The effect of different parameters such as electrode material and pH of the buffer solution on voltammetric response of sensors to HVA and VMA were studied. The sensor achieved LoD from different sensing materials varied from 0.6-1.2 μM for HVA and 0.4 - 2.4 μM for VMA. Also, the recorded limits of quantification were sufficient for determination of HVA and VMA in urine [31].

Even though MoS_2 has been applied in different sensing applications, yet it has never been investigated in the detection of HVA. In our study, we therefore report a simple one-step synthesis method of MoS_2 nanosheets combined with pluronic F127 which is an amphiphilic non-ionic surfactant that has been widely explored for liquid-phase exfoliation of 2D materials [33–35] as well as a novel electrochemical sensor based on MoS_2-Pluronic F127 modified platinum electrodes for the detection of HVA in the presence of uric acid.

2. Materials and methods

2.1 Reagents and apparatus

Potassium nitrate (KNO_3), potassium phosphate dibasic (K_2HPO_4), potassium phosphate monobasic (KH_2PO_4), potassium hexacyanoferrate(II) trihydrate ($K_4[Fe(CN)_6]•3H_2O$), creatinine (CR), molybdenum(IV) sulfide, pluronic F127, uric acid (UA), urea (UR), citric acid (CA) and ascorbic acid (AA) were supplied from Sigma Aldrich. HVA was purchased from Alfa Aesar of Thermo Fisher Scientific.

The morphology of MoS_2-F127 nanosheets was studied by transmission electron microscopy (TEM) and scanning electron microscopy (SEM) using FP 5022/22-Tecnai G2 20 S-TWIN and Nova Nano SEM-450 from Thermo Fisher Scientific. Surface image of MoS_2-F127 nanosheets was done using atomic force ICON (Bruker) microscope in tapping mode at a scanning rate of 0.9 Hz. The extinction and Raman spectra of bulk MoS_2 and MoS_2-F127 nanosheets were recorded with a UV-1800 spectrophotometer (Shimadzu, Japan) and a LabRAM HR evolution Raman spectrometer equipped with a 532 nm laser (Horiba), respectivel. X-ray diffraction (XRD) patterns of of the pluronic F127 and nanosheet powders were measured with a Rigaku SmartLab 9kW rotating anode X-ray diffractometer. PHI 5000 VersaProbe (ULVAC-PHI Inc., Hagisono, Chigasaki, Kanagawa, Japan) spectrometer was used to conduct XPS measurements under the following conditions: monochromatic Al Kα radiation ($h\nu$ = 1486.6 eV), an X-ray source operating at 25 W, 15 kV, 100 μm spot, pass energy of 23.5 eV, energy step of 0.1 eV. CasaXPS software was used to analyze the obtained XPS spectra using the set of the sensitivity factors native for the hardware. Shirley background and Gaussian-Lorentzian peak shape were used for deconvolution of all spectra. The thermal decomposition profiles of the pluronic F127 and nanosheet powders were obtained using a thermal gravimetric analyzer (Pyris 1 TGA, PerkinElmer) operated in the temperature range of 25 – 700 °C at a heating rate of 10 °C/min under nitrogen atmosphere. Cyclic voltammetry (CV), electrochemical impedance spectroscopy (EIS), and DPV were performed using an Ivium stat electrochemical workstation (Ivium Technologies, Ivium Stat, Netherlands) in a conventional three-electrode system. A bare platinum (Pt) electrode (2 mm in diameter, ItalSens) was used as working electrode, silver/silver chloride (Ag/AgCl) electrode, and Pt wire were used as reference and counter electrode, respectively.

2.2 Preparation of MoS_2-F127

MoS_2-F127 nanosheets were prepared at large scale using a kitchen blender through the process of shear exfoliation (**Scheme 1**) [32]. MoS_2 powder was added to 1 L of deionized water at a concentration of 50 mg/mL, followed by the addition of pluronic F-127 into the solution at a concentration of 10 mg/mL. The mixture was stirred for 10 mins to ensure proper mixing of the components. It was then transferred to the jug of a power blender (Inalsa MERAK 2000W) and exfoliated at a speed of 9000 rpm for 120 mins. To prevent overheating of the solution and the motor, an on/off (5/5 min) cycle was applied. After 120 mins of shear exfoliation, the solution was centrifuged at 1500 rpm for 90 mins. The supernatant carrying the exfoliated nanosheets was carefully collected, and the pellet was discarded. The collected supernatant was further subjected to 3 cycles of washing (10,000 rpm for 10 mins) using deionized water to remove excess Pluronic from the solution. The washed sample was finally redispersed in deionized water and used for subsequent experiments.

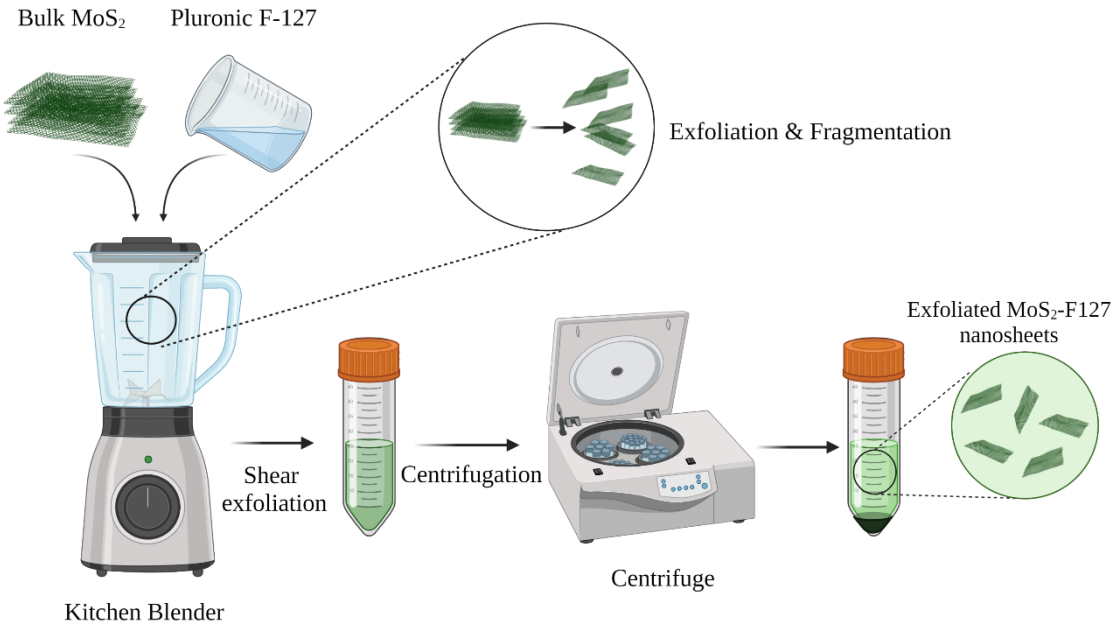

Scheme 1: Synthesis of Pluronic F-127 modified MoS_2 nanosheets through shear exfoliation technique using a kitchen blender.

2.3 Preparation of Pt/MoS_2-F127

Pt electrode was polished on a polishing pad containing alumina powders of 1, 0.3, and 0.05 µm in diameter. The electrode was then cleaned ultrasonically for 10 mins with ethanol and distilled water and air-dried at room temperature. Meanwhile, the MoS_2-F127 solution was vortexed for 5 min to obtain a homogeneous suspension. Finally, 20 µL of MoS_2-F127 was

added to the surface of the Pt electrode and placed at room temperature until the solvent was completely volatilized.

2.4 Electrochemical sensing

1 M KNO_3 solution was prepared by dissolving 2.52 g of KNO_3 in 25 mL of MilliQ water. Similarly, 0.1 M phosphate buffer solution (PBS) was prepared by dissolving 2.336 g of K_2HPO_4 and 1.577 g of KH_2PO_4 in 250 mL of MilliQ water.

Electrochemical behavior of Pt/MoS_2-F127 was studied either with 5×10^{-3} M solution of $Fe(CN)_6^{4-}$ prepared in 1 M KNO_3 solution or with 5×10^{-3} M HVA solution prepared in 0.1 M PBS. Cyclic voltammograms were measured in a potential range of -100 – 600 mV for $Fe(CN)_6^{4-}$ and -200 – 800 mV for HVA using five different scan rates 5, 10, 25, 50 and 100 $mV.s^{-1}$. EIS spectra were measured using 5×10^{-3} M solution of $Fe(CN)_6^{4-}$ in bare Pt, 1 layer, 2 layers and 3 layers of MoS_2. The frequency range was swept from 100 kHz – 0.1 Hz with an amplitude of 0.005 V and a polarization potential of -3 mV.

Effect of the number of MoS_2-F127 layers on the oxidation peak of HVA was examined using bare Pt, 1 layer, 2 layers and 3 layers of MoS_2-F127 with 5×10^{-3} M HVA solution prepared in 0.1 M PBS. DPV curves of HVA were measured between -200 – 800 mV using a scan rate of 5 $mV.s^{-1}$.

Resolution between HVA and UA was examined in their mixed solution by DPV using Pt and Pt/MoS_2-F127. The concentration of UA was fixed at 200 µM while the concentration of HVA was varied between 50, 100, and 200 µM in particular. DPV was also used to study the effect of other interfering compounds, including AA, CA, UR, and CR, on the detection of HVA. Solutions of HVA, AA, CA, UR, and CR were prepared at six concentrations of 50, 500, 100, 2000, 4000, and 5000 µM, while UA was prepared at five different concentrations ranging from 50, 100, 200, 300 to 350 µM. The choice of this range was due to the solubility of UA. DPV curves were recorded between -200 – 800 mV using a scan rate of 5 $mV.s^{-1}$.

3. Results and discussion

3.1 Synthesis and characterization of MoS_2-F127 nanosheets

The method of surfactant-assisted shear exfoliation of 2D materials was adopted in this work to synthesize MoS_2 nanosheets at a large scale [32]. The process of shear mixing involves the use of mixers or blenders that contain a motor-driven rotor/blade. The rotation of these blades

at a fixed speed generates large shear forces in the vicinity of the suspended materials, which helps in exfoliating them into mono- to few-layered sheets. The addition of an intercalating agent, such as a surfactant into this process further helps in improving the efficiency of exfoliation and also provides colloidal stability to the exfoliated sheets through surface functionalization. In this work, bulk MoS_2 was exfoliated into nanosheets in the presence of an aqueous surfactant solution of Pluronic F-127, using a simple kitchen blender as the shear mixing apparatus. Pluronic F-127 is an amphiphilic non-ionic surfactant that has been widely explored for liquid-phase exfoliation of 2D materials [33–35]. The process of liquid-phase exfoliation of MoS_2 using Pluronic F-127 involves both hydrophilic and hydrophobic interactions between the surfactant and the 2D material. MoS_2 being hydrophobic in nature allows the surfactant molecules to interact with its surface through the hydrophobic sections of the surfactant. This helps the surfactant molecules to intercalate between the layers of the bulk MoS_2 and adhere to the surface. On the other hand, the hydrophilic section of the surfactant interacts with water molecules to render colloidal stability to MoS_2 in aqueous environment. The process of intercalation weakens the van der Waal's forces between MoS_2 layers, and as a result, in the presence of high shear forces, the material gets exfoliated easily. The exfoliated MoS_2 sheets are stabilized by a layer of Pluronic F-127 molecules adhering to its surface and thereby preventing re-aggregation through hydrophobic interactions, while maintaining aqueous stability through hydrophilic interactions.

The shear mixing of MoS_2 in aqueous Pluronic F-127 solution resulted in a dark colored liquid, which upon centrifugation, yielded a homogenous and dark green solution containing MoS_2-F127 nanosheets. Microscopic evaluation of the as-synthesized nanosheets using TEM (**Fig. 1A-C**) and SEM (**Fig. 1D**) clearly revealed uniform and well dispersed two-dimensional nanostructures resembling sheets. As shown in **Fig. 1A-B**, the TEM micrographs show a well-defined lamellar morphology of the nanosheets without any signs of aggregation. The presence of few-layered nanosheets can be seen from these TEM images. The HR-TEM image shown in **Fig. 1C** depicts the highly crystalline nature of the exfoliated nanosheets, which is also supported by the hexagonal atomic arrangement of MoS_2 as observed from the selected area (electron) diffraction (SAED) pattern (**Fig. 1C**, inset). SEM analysis (**Fig. 1D**) corroborates the above observations and shows the presence of MoS_2 nanosheets having size in the range of 150-200 nm. Thus, the process of shear mixing generates uniformly dispersed and exfoliated MoS_2 nanosheets of a highly crystalline nature. The average thickness of the synthesized nanosheets as determined from the AFM images is ~4.45 nm (**Fig. 1E-F**). Assuming a

thickness of 1–1.5 nm for a single layer and taking into account the adsorbed pluronic on both sides of the nano-sheet, the average number of layers is expected to be between 3-4.

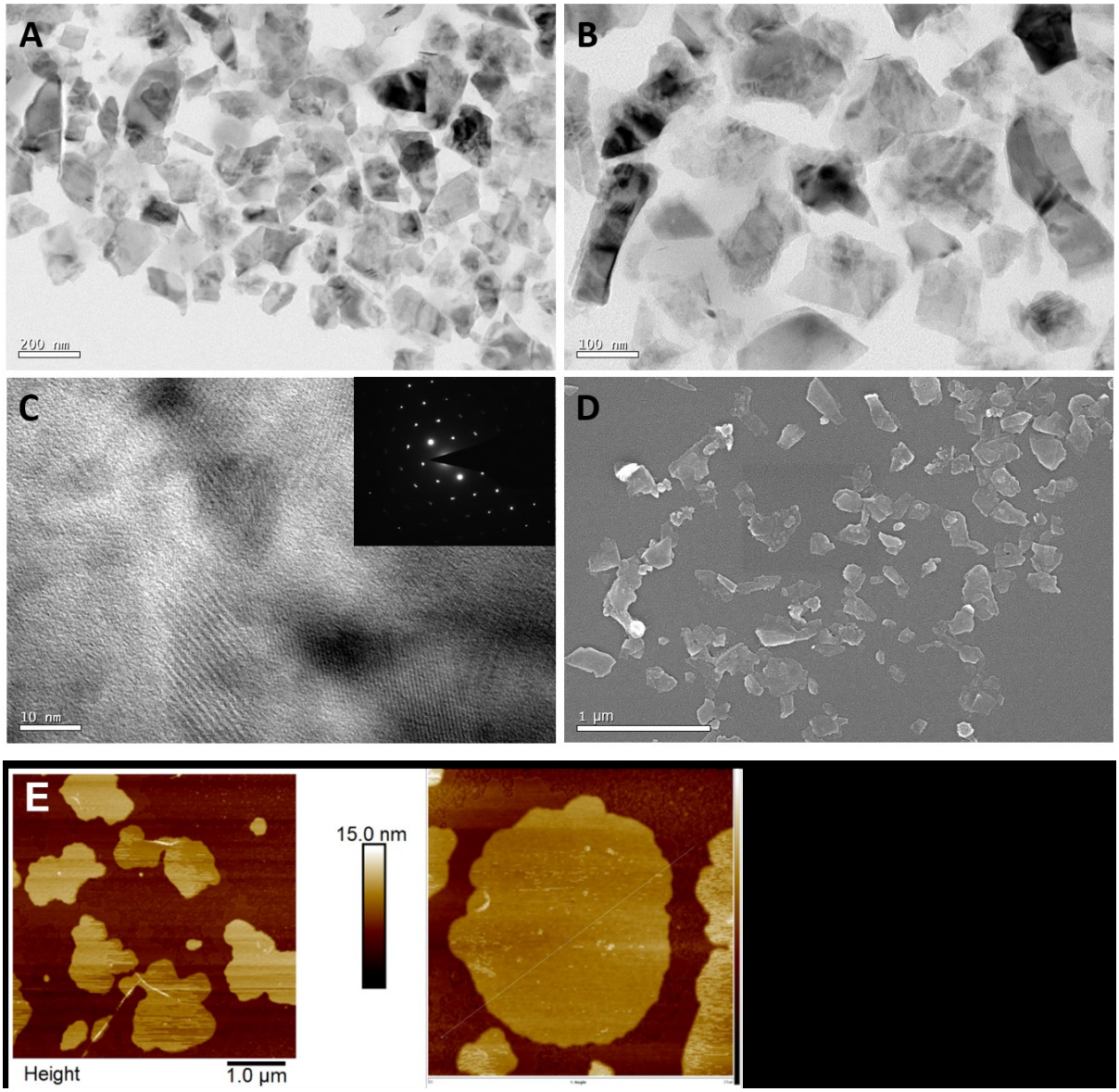

Figure 1. *Morphological characterization of MoS_2-F127 nanosheets. (A-B) TEM, (C) HR-TEM & SAED (inset), (D) SEM images of MoS_2-F127 nanosheets. (E) AFM images of MoS_2-F127 nanosheets along with (F) their height profile showing the thickness of the nanosheets.*

The chemical nature of the synthesized nanosheets can be confirmed using a number of characterization tools. To begin with, we analyzed the extinction spectra (**Fig. 2A**) of the as-synthesized MoS_2-F127 nanosheets and observed the appearance of characteristic excitonic transitions at 400 nm, 450 nm, 610 nm, and 670 nm, consistent with the 2H-polytype of MoS_2 [36–38]. Raman spectroscopy of the synthesized material revealed further information about the molecular nature of the layered material. As can be seen from **Fig. 2B**, the Raman spectra of bulk MoS_2 shows two characteristic phonon modes at 375.91 cm^{-1} (E^1_{2g}) and 402.44 cm^{-1}

(A_{1g}) arising from the in-plane opposite vibrations of sulfur/molybdenum atoms and out-of-plane vibrations of sulfur atoms, respectively [37,38]. As the number of layers in the bulk MoS_2 decreases on account of exfoliation, the E^1_{2g} and A_{1g} phonon modes shift towards higher wavenumbers along with a decrease in the frequency difference between these two modes compared to bulk MoS_2 [38]. The Raman spectra of MoS_2-F127 nanosheets clearly show the shifting of the E^1_{2g} and A_{1g} phonon modes to higher wavenumbers. Also, the frequency difference between these two modes for MoS_2-F127 nanosheets was calculated to be 24.96 cm^{-1}, which was lower than that of bulk MoS_2 (26.19 cm^{-1}). Thus, the Raman data establishes the exfoliated nature of the as-synthesized MoS_2-F127 nanosheets. XRD analysis of MoS_2-F127 nanosheets also supports the above results. As shown in **Fig. 2C**, the XRD spectra of bulk MoS_2 show multiple sharp diffraction peaks corresponding to different lattice planes (JCPDS Card No. 37-1492). The sharp peak at $2\theta = 14.4°$ in bulk MoS_2 corresponds to (002) plane, which was found to be decreased in intensity as well as broadened in the case of MoS_2-F127 nanosheets. The reduction in peak intensity, along with peak broadening further confirms the exfoliated nature of MoS_2-F127 nanosheets [37]. Surface functionalization of MoS_2 nanosheets using F127 was confirmed from TGA analysis (**Fig. 2D**). Bulk MoS_2 showed weight loss between 300 - 550ºC due to degradation of the oxidized molybdenum species such as MoO_3 present on the nanosheet surface on account of mild oxidation during aqueous phase exfoliation and storage [37]. MoS_2-F127 nanosheets depict a thermal decomposition profile that consists of a sharp decrease in weight from 200 - 300 ºC arising from the degradation of pluronic F-127 molecules [39]. This is followed by a mild weight loss from 300 - 400 ºC pertaining to degradation of oxidized molybdenum species similar to what was observed in case of pristine MoS_2, thereby establishing the presence of pluronic molecules on the surface of MoS_2 nanosheets which was calculated to be ~ 36 wt% of MoS_2. X-ray photoelectron measurement was used to confirm the chemical composition of the studied material. The high-resolution XPS spectra of sulfur S 2p and Mo 3d are shown in **Fig. 2E-F**, accordingly. Due to spin-orbit coupling, signals for both sulfur and molybdenum are present as doublets (Mo 3d 5/2 and Mo 3d 3/2 separated by 3.1 eV and S 2p 3/2 and S 2p 1/2, separated by 1.2 eV). The peak position of the Mo3d5 and S2p3 is very typical for MoS_2 compound and agrees perfectly with literature data [40–42]. No other chemical states of the sulfur and molybdenum are observed.

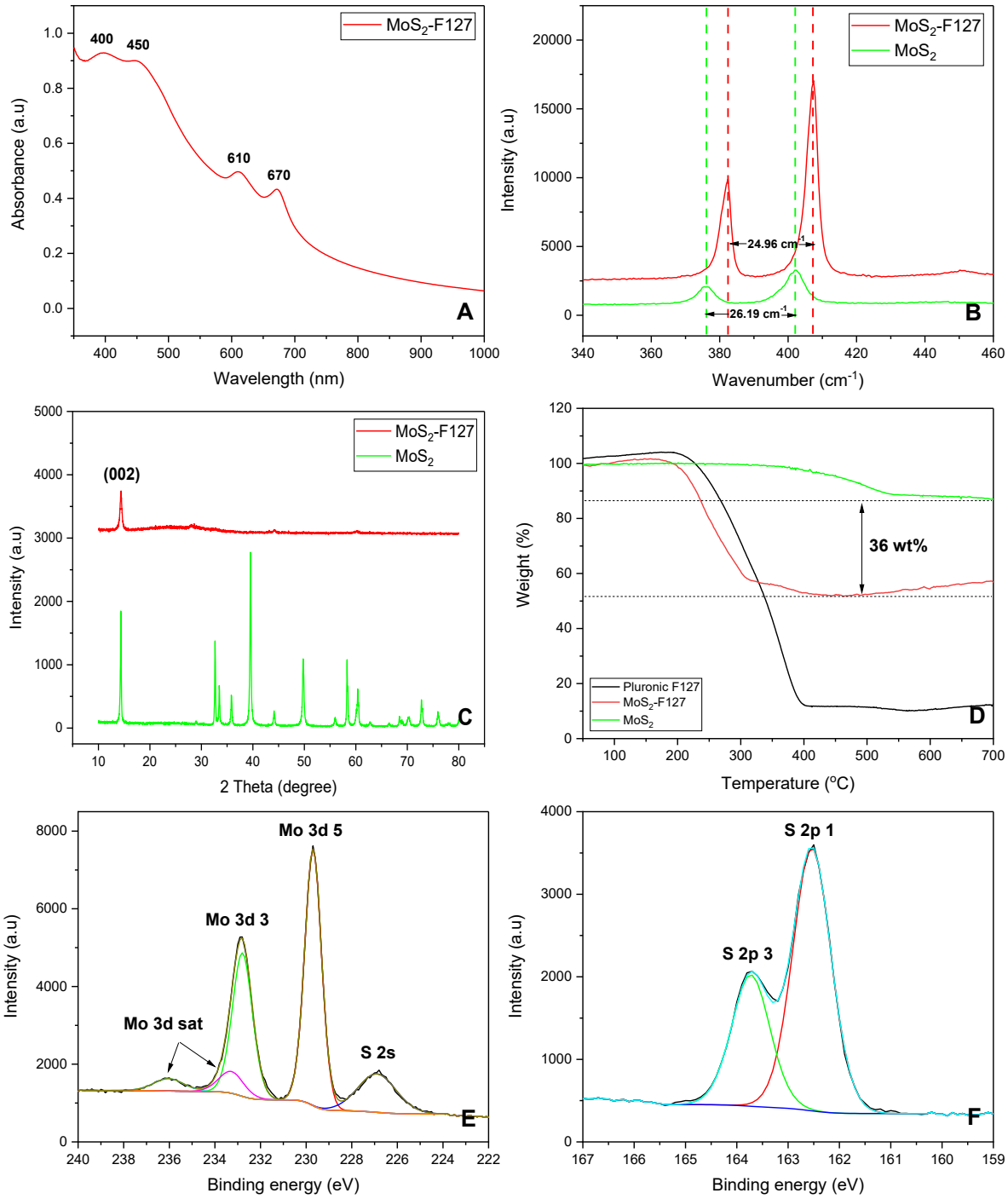

Figure 2. *(A) Extinction spectra of MoS_2-F127 nanosheets, (B) Raman spectra of bulk MoS_2 and MoS_2-F127 nanosheets, (C) XRD pattern of bulk MoS_2 and MoS_2-F127 nanosheets, (D) TGA curves of bulk MoS_2 and MoS_2-F127 nanosheets (E) XPS spectrum of Mo 3d region and (F) XPS spectrum of S2p region.*

3.2 Electrochemical characterization of Pt/MoS_2-F127

In an attempt to study the electrochemical properties of Pt/MoS_2-F127, the bare Pt and modified electrode Pt/MoS_2-F127 were characterized using cyclic voltammetry (CV) in 1 M KNO_3 solution containing 5×10^{-3} M $Fe(CN)_6^{4-}$. **Fig. 3** shows the CV curves of $Fe(CN)_6^{3-/4-}$ on Pt

(a) and Pt/MoS_2-F127 (b). Both figures indicate the presence of a redox peak on both Pt and Pt/MoS_2-F127, which relates to the redox reactions of $Fe(CN)_6^{3-/4-}$. It can be seen that the redox peak current of $Fe(CN)_6^{3-/4-}$ at Pt is higher than that at Pt/MoS_2-F127, indicating that MoS_2-F127 decreased the electron transfer. The diffusion coefficient was also calculated using Randles-Sevcik equation shown below. The slope of the calibration curve of the current and the scan rate shown in **Fig. 3D** was used to calculate the diffusion coefficient and was found to be 3.36×10^{-5} cm^2/s.

$$i_p = 0.4463AC\left(\frac{n^3F^3vD}{RT}\right)^{1/2} \qquad (1)$$

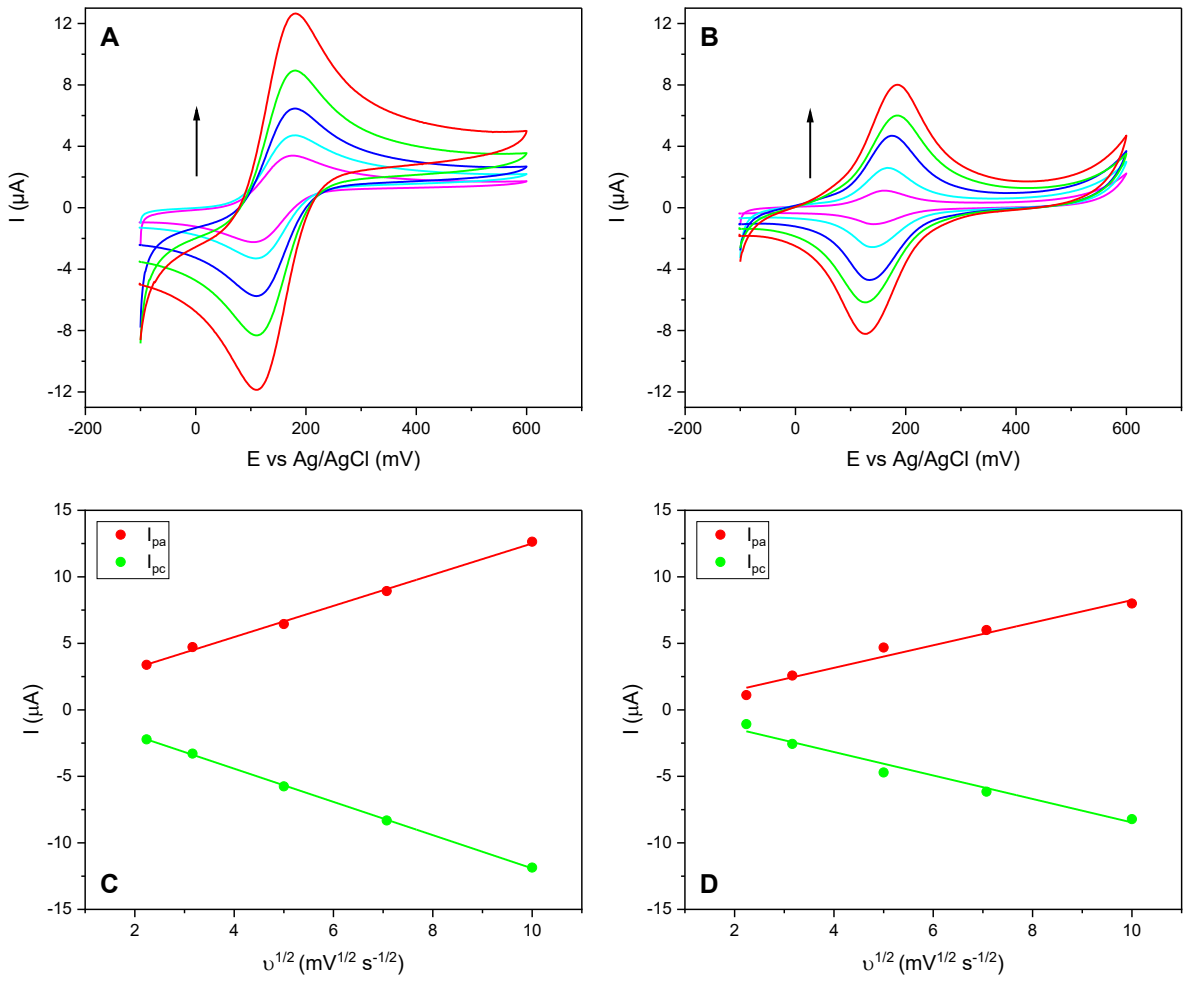

Figure 3. *Cyclic voltammogram of 5 × 10^{-3} M $Fe(CN)_6^{3-/4-}$ in 1 M KNO_3 recorded at the (A) Pt and (B) Pt/MoS_2-F127 electrodes at different scan rates (the order following the direction of the arrow). Current (I) vs. square root of the scan rate ($v^{1/2}$) in (C) Pt and (D) Pt/MoS_2-F127. Scan rate: 5, 10, 25, 50, 100 mV.s^{-1}.*

3.3 Electrochemical sensor for HVA

3.3.1 Effect of the scan rate

Fig. 4 displays the effect of scan rate on the peak current of HVA on both Pt and Pt/MoS_2-F127 using five scan rates. Both figures indicate the presence of an oxidation peak of HVA, which increases when the scan rate increases. **Fig. S1** shows the CV curves of 0.1 M PBS in both Pt and Pt/MoS_2-F127, proving that the anodic peak found in **Fig. 4** is indeed due to the oxidation of HVA. However, the cathodic peak current of HVA is not visible, indicating that HVA undergoes an irreversible reaction. They also highlight the difference between the cyclic voltammogram of HVA in Pt and Pt/MoS_2-F127. The oxidation peak of HVA is more pronounced in Pt compared to Pt/MoS_2. Also, the oxidation potential of HVA shifts from lower to higher potentials when modifying Pt with MoS_2-F127.

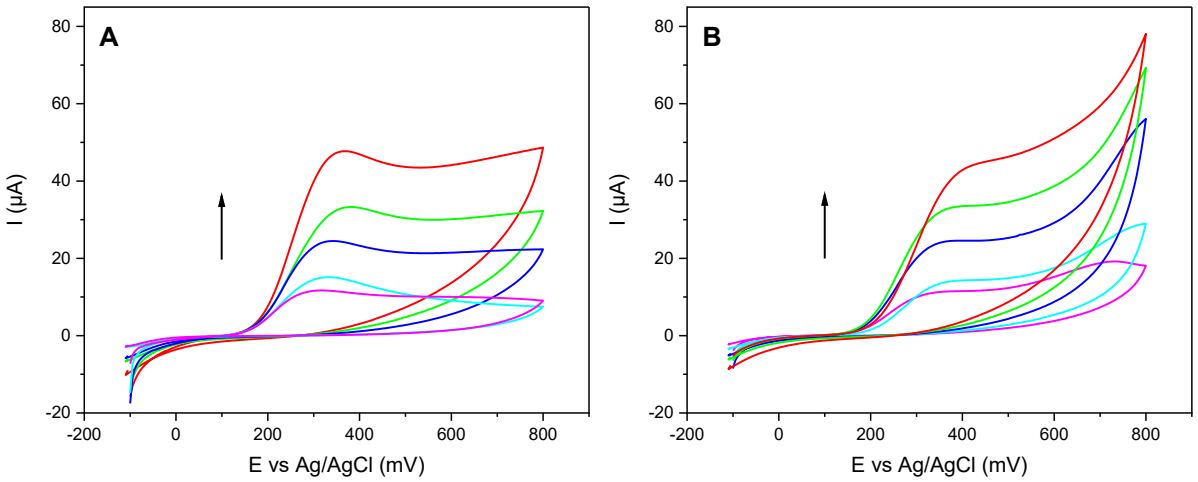

Figure 4. *Cyclic voltammograms of 5 × 10^{-3} M HVA in 0.1 M PBS recorded at (A) Pt and (B) Pt/MoS_2-F127 electrode. Scan rate: 5, 10, 25, 50, 100 mV.s^{-1} (the order following the direction of the arrow).*

The number of electrons *n* involved in the oxidation reaction of HVA by the Pt/MoS_2-F127 electrode was calculated using Laviron equation (Eqn. 2) [43],

$$E_p = E^{0'} - \frac{RT}{\alpha nF} ln \frac{RTK_s}{\alpha nF} + \frac{RT}{\alpha nF} \ln v \qquad (2)$$

where E_p and $E^{0'}$ is the peak potential and surface standard potential and K_S is the standard heterogeneous reaction rate constant; α refers to charge transfer coefficient; *v* is potential scan rate, *R*, *T*, and *F* are gas constant, absolute temperature, and Faraday constant, respectively.

When plotting E_p versus ln$v$, the slope of the linear curve (**Fig. S2**) is equal to RT/αnF from Eqn. 2. As we have an irreversible oxidation of HVA, the α coefficient is usually taken as 0.4–0.6 [31] and n is found to be 2. Therefore, the chemical oxidation of HVA involves two electrons and one proton [44] as depicted in **Fig. 5**.

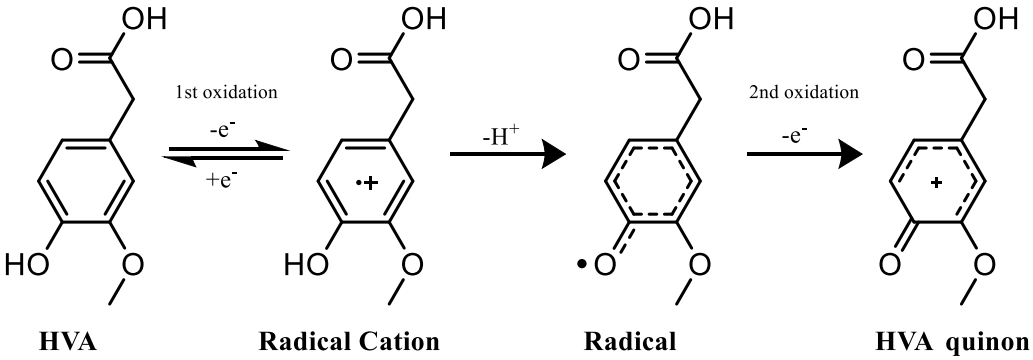

Figure 5. *Electrochemical oxidation mechanism of HVA* [44].

3.3.2 Effect of the coating

Three different Pt electrodes were coated with 20, 40, and 60 µL of MoS_2-F127 in order to study the effect of the coating on the HVA peak current. Electrochemical impedance spectroscopy (EIS) was also used to characterize the effect of the increasing number of MoS_2-F127 layers. **Fig. 6A** displays the Nyquist plot of Pt as well as three different MoS_2-F127 coatings. Pt shows a straight line representing a double-layer capacitor which behaves like a constant phase element (CPE). Unlike Pt/MoS_2-F127, which displays an extra semi-circle corresponding to the interfacial electron transfer resistance. The diameter of the semi-circle becomes more visible when the number of MoS_2-F127 layers increases, implying that the increasing number of coatings decreased electron transfer resistance of the electrode.

Fig 6B. illustrates the DPV curves of HVA measured in bare Pt, 1 layer, 2 layers, and 3 layers of MoS_2-F127. Moreover, it shows that the current peak of HVA on the bare Pt is higher than that on the three different coatings of MoS_2-F127, confirming the results obtained from CV and EIS in solutions of redox probe and buffer. Furthermore, the HVA peak intensity decreases and shifts from higher to lower potentials when the number of MoS_2-F127 layers increases. Consequently, we chose to continue our further experiments with 1 layer of MoS_2-F127 (Pt/1L-MoS_2-F127) due to its slightly higher peak current and shifted oxidation potential. The figure also shows a second peak around an oxidation potential of 600 mV which is due to the oxidation of the Pluronic F-127 polymer. Its oxidation potential also shifts marginally from

higher to lower potentials when the number of MoS_2-F127 layers increases, validating the shifting characteristic of MoS_2-F127.

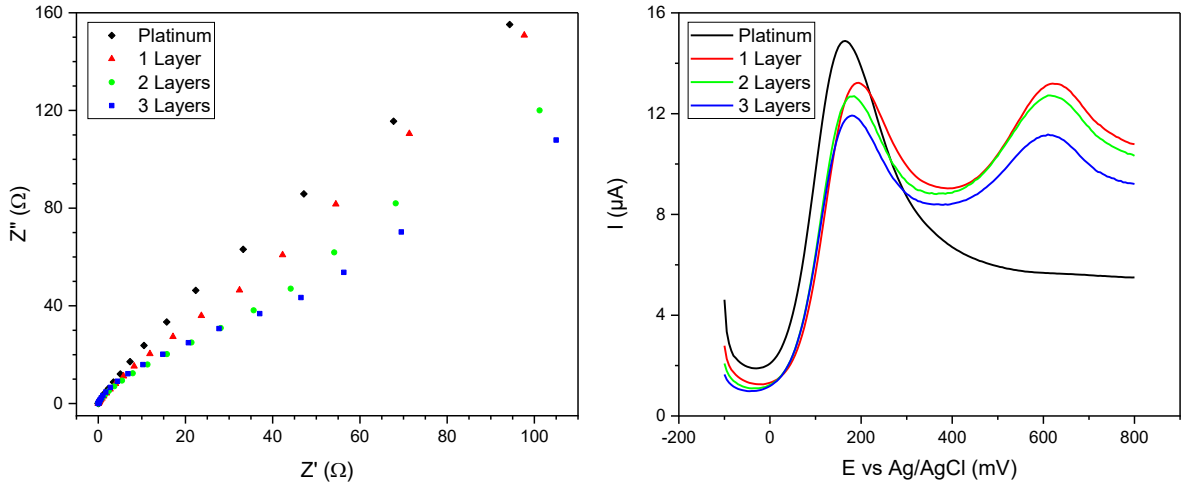

Figure 6. *(A) EIS curves of 1 M KNO_3 containing 5.0 × 10^{-3} M $Fe(CN)_6^{4-}$ recorded at the bare Pt electrodes and Pt electrode coated with different layers of MoS_2-F127. Polarization potential: −0.003 V, Frequency range: 100 kHz - 0.1 Hz, Amplitude: 0.005 V. (B) DPV curves of HVA in bare Pt, 1 layer, 2 layers, and 3 layers of MoS_2-F127. Scan rate: 5 mV.s^{-1},*

3.4 Interference study

The selectivity of Pt/1L-MoS_2-F127 towards HVA was studied using DPV using five interfering substances, including UA, AA, CA, UR, and CR. The choice of these molecules was based on their interfering capabilities. For instance, interference of AA on urine test strip analysis has been known for many years. On the other hand, CA, UA, UR, and CR were selected based on their higher abundance in urine [45–47].

Fig. 7 represents the DPV curves of HVA and UA at three different concentration ratios (1:4, 1:2 and 1:1 HVA:UA). **Fig. S3** shows the baseline-corrected DPV curves of HVA and UA. The peak current of HVA increases proportionally with the increasing concentration, while the peak current of UA is nearly constant due to its fixed concentration. It can be seen that the HVA peak current is visible at a concentration of 50 μM and the resolution between

the two compounds is fairly obvious. Thus, showing the ability of Pt/1L-MoS_2-F127 to simultaneously detect HVA and UA.

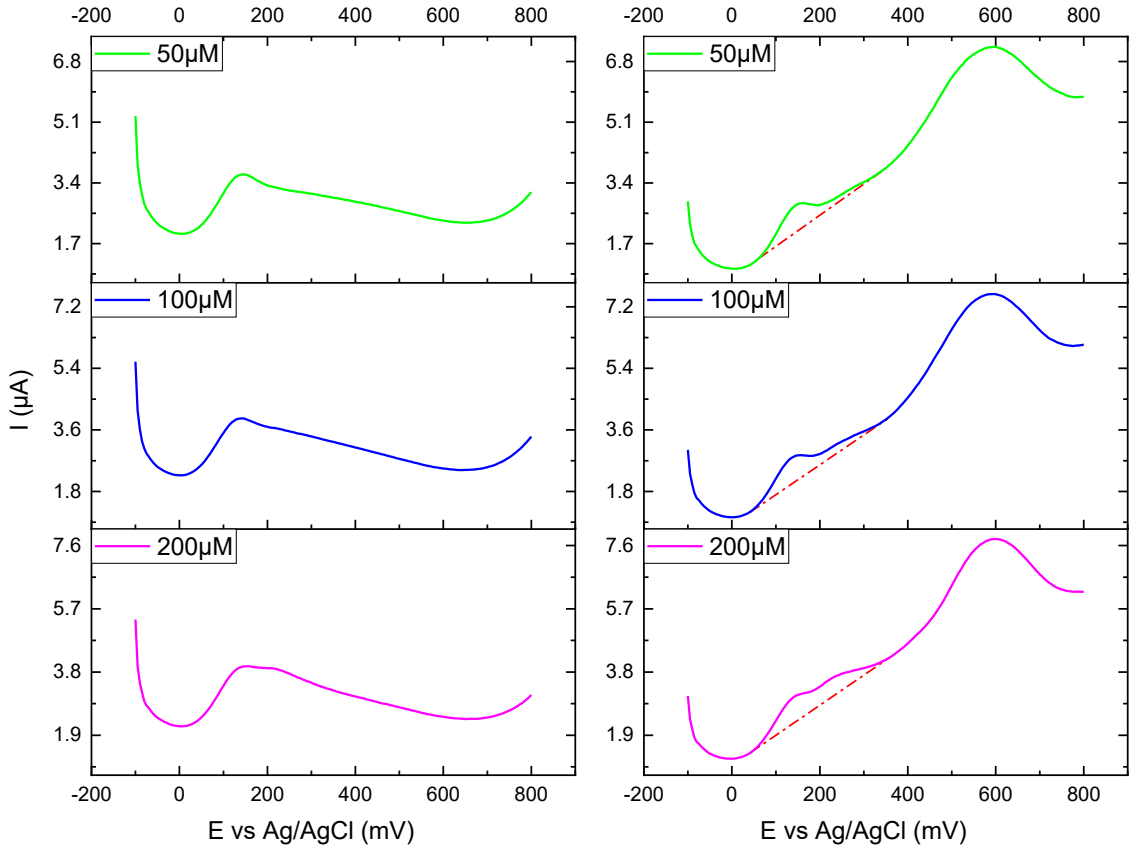

Figure 7. *DPV curves of HVA and UA in Pt (left) and Pt/1L-MoS_2-F127 (right) in 0.1 M PBS (pH 7.0) at a fixed concentration of UA (200 μM).*

Fig. 8 shows the calibration curves of the peak current of HVA, CR, UR, CA, AA as well as UA at different concentrations ranging from 50 – 5000 μM and 50 – 350 μM, respectively. The LoD for HVA was calculated using the following formulae: $LoD = \frac{3s}{m}$ where 'm' is the slope of the calibration curve of HVA, and 's' is the standard deviation of the three current responses measured using three 0.1 M PBS solutions and was found to be 9.76 μM. The peak currents of HVA and UA increase proportionally when the concentration increases. It also indicates that the peak current of HVA and UA increase rapidly compared to a nearly constant current obtained from the other interfering substances. In addition, the calibration curves of HVA and UA give similar peak currents at 350 μM, but the resolution between the two peaks is quite evident, as shown in **Fig. 7**. Furthermore, the DPV curves of AA, CA, UR, and CR did not show any oxidation peaks around an oxidation potential of 290 mV where HVA oxidizes, proving that AA, CA, UR, and CR do not alter the detection of HVA, i.e., these results

demonstrate significant selectivity of the sensor to HVA. For instance, by dividing the slope of HVA by the one of AA [48], the calculated selectivity of the sensor to HVA is ~six-fold higher than that to AA.

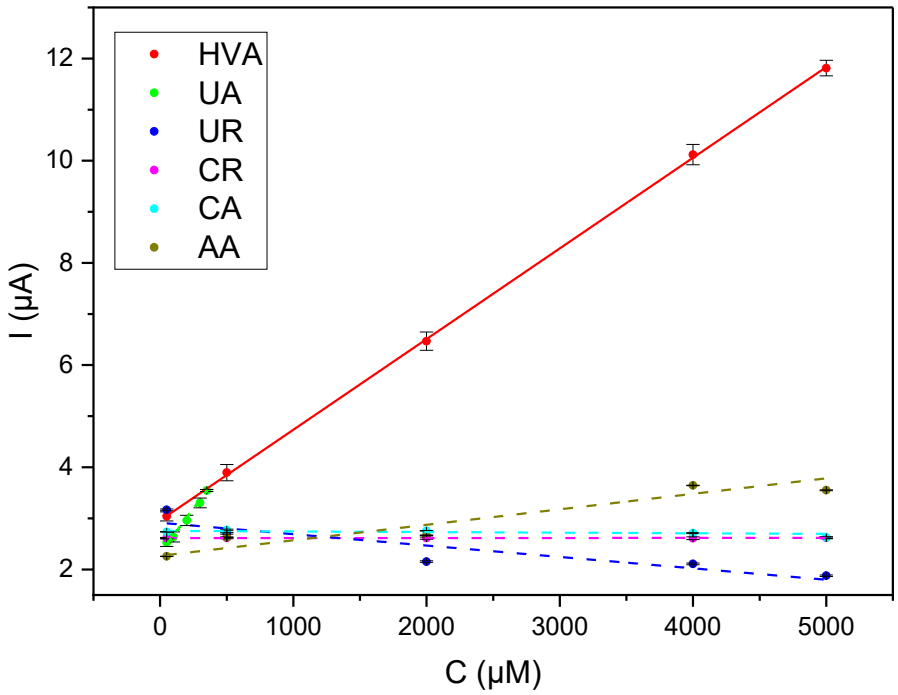

Figure 8. *Selectivity of Pt/1L-MoS_2-F127 towards HVA compared to UA, CA, AA, CR and UR.*

Table 1. *Comparison of the response characteristics of different methods for HVA detection.*

Electrode	Method	Linear range (× 10^{-6} M)	LOD (× 10^{-6} M)	Reference
Pluronic-modified MoS_2/Pt	DPV	50-5000	9.76	This work
Screen-printed	DPV	0.8-100	0.24	[49]
Boron doped diamond	DPV	2-100	0.6	[31]
Composite carbon film	DPV	0.8-100	0.1	[50]
Cu/GC	OSWV*	-	0.01	[51]
MWCNT-PtNPs/GCE	DPV	0.2-80	0.08	[27]

*OSWV - Osteryoung square wave voltammetry

Table 1. shows the linear calibration ranges and LoD of HVA between different reported methods. Although this study reports a higher LoD compared to other work, a much wider calibration range, 50 – 5000 μM, was achieved in this work. This may extend potential

applications of the sensor to other fields. It is worth mentioning that this study also investigates the detection of HVA in the presence of UA which oxidizes near HVA.

4. Conclusion

A number of previously reported studies on the electrochemical detection of HVA focused mainly on particular interfering compounds, unlike this paper which investigates the detection of HVA in the presence of uric acid (UA) using MoS_2 combined with Pluronic F127. The material was synthesized at large scale using a kitchen blender through the process of surfactant-assisted shear exfoliation. TEM and SEM showed consistent and highly dispersed 2D nanostructures resembling sheets. UV-VIS and Raman spectra showed characteristic excitonic transitions of the 2H-polytype MoS_2 and phonon modes arising from the in-plane opposite vibrations of sulfur/molybdenum atoms and out-of-plane vibrations of sulfur atoms, respectively. Moreover, TGA analysis confirmed the presence of pluronic F127 molecules on the surface of MoS_2 with an approximate weight percentage of ~ 36 wt% of MoS_2. Lastly, XPS and XRD measurements were used to confirm the chemical composition of the synthesized material. MoS_2-F127 was then used for the study of HVA and UA. The as-fabricated sensor showed a wide dynamic range of 50 – 5000 μM, acceptable LoD of 9.76 μM, high sensitivity towards HVA in the presence of ascorbic acid, citric acid, creatinine and urea, and importantly a good resolution between HVA and UA. Finally, the current fabrication procedure of the sensor could be extended for making flexible/stretchable sensors.

Acknowledgments

T.-P. Huynh acknowledges the Liv och Hälsa Foundation and the Academy of Finland (Grant No. 323240 and 331774) for financial support. All authors acknowledge the INDFICORE (Indian Finnish Consortia for Research and Education). AJ acknowledges the support from BioX centre and Advanced Materials Research Centre (AMRC), Indian Institute of Technology Mandi for research and infrastructure facility.

References

[1] Hu H, Zavabeti A, Quan H, Zhu W, Wei H, Chen D and Ou J Z 2019 Recent advances in two-dimensional transition metal dichalcogenides for biological sensing *Biosens. Bioelectron.* **142** 111573

[2] Yadav V, Roy S, Singh P, Khan Z, Jaiswal A, Yadav V, Roy S, Singh P, Jaiswal A and Khan Z 2019 2D MoS2-Based Nanomaterials for Therapeutic, Bioimaging, and Biosensing Applications *Small* **15** 1803706

[3] Pollmann E, Madauß L, Zeuner V and Schleberger M 2018 Strain in Single-Layer MoS2 Flakes Grown by Chemical Vapor Deposition *Encycl. Interfacial Chem. Surf. Sci. Electrochem.* 338–43

[4] Geng D, Bo X and Guo L 2017 Ni-doped molybdenum disulfide nanoparticles anchored on reduced graphene oxide as novel electroactive material for a non-enzymatic glucose sensor *Sensors Actuators B Chem.* **244** 131–41

[5] Fang L, Wang F, Chen Z, Qiu Y, Zhai T, Hu M, Zhang C and Huang K 2017 Flower-like MoS2 decorated with Cu2O nanoparticles for non-enzymatic amperometric sensing of glucose *Talanta* **167** 593–9

[6] Parlak O, İncel A, Uzun L, Turner A P F and Tiwari A 2017 Structuring Au nanoparticles on two-dimensional MoS2 nanosheets for electrochemical glucose biosensors *Biosens. Bioelectron.* **89** 545–50

[7] Lin X, Ni Y and Kokot S 2016 Electrochemical cholesterol sensor based on cholesterol oxidase and MoS2-AuNPs modified glassy carbon electrode *Sensors Actuators B Chem.* **233** 100–6

[8] Mani V, Govindasamy M, Chen S-M, Karthik R and Huang S-T 2016 Determination

of dopamine using a glassy carbon electrode modified with a graphene and carbon nanotube hybrid decorated with molybdenum disulfide flowers *Microchim. Acta 2016 1837* **183** 2267–75

[9] Catalán-Gómez S, Briones M, Cortijo-Campos S, García-Mendiola T, de Andrés A, Garg S, Kung P, Lorenzo E, Pau J L and Redondo-Cubero A 2020 Breast cancer biomarker detection through the photoluminescence of epitaxial monolayer MoS2 flakes *Sci. Reports 2020 101* **10** 1–9

[10] Alarfaj N A, El-Tohamy M F and Oraby H 2018 New label-free ultrasensitive electrochemical immunosensor-based Au/MoS2/rGO nanocomposites for CA 27-29 breast cancer antigen detection *New J. Chem.* **42** 11046–53

[11] Hu T, Zhang M, Wang Z, Chen K, Li X and Ni Z 2020 Layer-by-layer self-assembly of MoS2/PDDA hybrid film in microfluidic chips for ultrasensitive electrochemical immunosensing of alpha-fetoprotein *Microchem. J.* **158** 105209

[12] Yan R, Lu N, Han S, Lu Z, Xiao Y, Zhao Z and Zhang M 2022 Simultaneous detection of dual biomarkers using hierarchical MoS2 nanostructuring and nano-signal amplification-based electrochemical aptasensor toward accurate diagnosis of prostate cancer *Biosens. Bioelectron.* **197** 113797

[13] Yang Y, Zeng B, Li Y, Liang H, Yang Y and Yuan Q 2020 Construction of MoS2 field effect transistor sensor array for the detection of bladder cancer biomarkers *Sci. China Chem. 2020 637* **63** 997–1003

[14] Ferlay J, Ervik M, Lam F, Colombet M, Mery L, Piñeros M, Znaor A, Soerjomataram I and Bray F 2020 Global cancer observatory: cancer today. Lyon: International Agency for Research on Cancer; 2018

[15] Mitra S, Ganguli S and Chakrabarti J 2018 Introduction *Cancer and Noncoding RNAs* (Elsevier) pp 1–23

[16] Sadana A and Sadana N 2015 Detection of Cancer Biomarkers on Biosensor Surfaces *Biomarkers Biosens.* 43–108

[17] Henry N L and Hayes D F 2012 Cancer biomarkers *Mol. Oncol.* **6** 140–6

[18] Lambert G W, Eisenhofer G, Jennings G L and Esler M D 1993 Regional homovanillic acid production in humans *Life Sci.* **53** 63–75

[19] Guneral F and Bachmann C 1994 Age-related reference values for urinary organic acids in a healthy Turkish pediatric population. *Clin. Chem.* **40** 862–6

[20] Muñoz-González I, Jiménez-Girón A, Martín-Álvarez P J, Bartolomé B and Moreno-Arribas M V 2013 Profiling of microbial-derived phenolic metabolites in human feces after moderate red wine intake *J. Agric. Food Chem.* **61** 9470–9

[21] Espino A, Calopa M, Ambrosio S, Ortolà J, Peres J and Navarro M A 1995 CSF somatostatin increase in patients with early parkinsonian syndrome *J. Neural Transm. Park. Dis. Dement. Sect.* **9** 189–96

[22] Alfredsson G and Wiesel F A 1989 Monoamine metabolites and amino acids in serum from schizophrenic patients before and during sulpiride treatment *Psychopharmacology (Berl).* **99** 322–7

[23] Slupsky C, H S, TH W, K D, A S, V C, W F and MB S 2010 Urine metabolite analysis offers potential early diagnosis of ovarian and breast cancers *Clin. Cancer Res.* **16** 5835–41

[24] Bax C, Lotesoriere B J, Sironi S and Capelli L 2019 Review and Comparison of Cancer Biomarker Trends in Urine as a Basis for New Diagnostic Pathways *Cancers (Basel).* **11**

[25] Hovancová J, Šišoláková I, Oriňaková R and Oriňak A 2017 Nanomaterial-based electrochemical sensors for detection of glucose and insulin *J. Solid State Electrochem. 2017 218* **21** 2147–66

[26] Pandey S K, Mohanta G C and Kumar P 2019 Development of Disposable Sensor Strips for Point-of-Care Testing of Environmental Pollutants *Adv. Nanosensors Biol. Environ. Anal.* 95–118

[27] Fu B, Chen H, Yan Z, Zhang Z, Chen J, Liu T and Li K 2020 A simple ultrasensitive electrochemical sensor for simultaneous determination of homovanillic acid and vanillylmandelic acid in human urine based on MWCNTs-Pt nanoparticles as peroxidase mimics *J. Electroanal. Chem.* **866** 114165

[28] Němečková-Makrlíková A, Matysik F-M, Navrátil T, Barek J and Vyskočil V 2019 Determination of three Tumor Biomarkers (Homovanillic Acid, Vanillylmandelic Acid, and 5-Hydroxyindole-3-Acetic Acid) Using Flow Injection Analysis with Amperometric Detection *Electroanalysis* **31** 303–8

[29] Guo S, Chen X, Ling Y, Wang H, Wei X, Pan R, Wang P and Road J 2021 Modification of a Carbon Paste Electrode with a ZnO@ZIF-8 Nanocomposite and Fabrication of a Highly Sensitive Electrochemical Sensor for Sulfamethoxazole Detection *Int. J. Electrochem. Sci* **16** 210950

[30] Hrdlička V, Barek J and Navrátil T 2021 Differential pulse voltammetric determination of homovanillic acid as a tumor biomarker in human urine after hollow fiber-based liquid-phase microextraction *Talanta* **221** 121594

[31] Baluchová S, Barek J, Tomé L I N, Brett C M A and Schwarzová-Pecková K 2018 Vanillylmandelic and Homovanillic acid: Electroanalysis at non-modified and polymer-modified carbon-based electrodes *J. Electroanal. Chem.* **821** 22–32

[32] Varrla E, Backes C, Paton K R, Harvey A, Gholamvand Z, McCauley J and Coleman J N 2015 Large-scale production of size-controlled MoS2 nanosheets by shear exfoliation *Chem. Mater.* **27** 1129–39

[33] Hu C X, Shin Y, Read O and Casiraghi C 2021 Dispersant-assisted liquid-phase

exfoliation of 2D materials beyond graphene *Nanoscale* **13** 460–84

[34] Kulkarni H B, Tambe P B and Joshi G M 2019 Influence of surfactant assisted exfoliation of hexagonal boron nitride nanosheets on mechanical, thermal and dielectric properties of epoxy Nanocomposites *https://doi.org/10.1080/09276440.2019.1663115* **27** 529–50

[35] Alamer M, Zamani S, Fok K, Satish A, Lim A R and Joo Y L 2020 Facile Production of Graphenic Microsheets and Their Assembly via Water-Based, Surfactant-Aided Mechanical Deformations *ACS Appl. Mater. Interfaces* **12** 8944–51

[36] Kumar P, Roy S, Sarkar A and Jaiswal A 2021 Reusable MoS2-Modified Antibacterial Fabrics with Photothermal Disinfection Properties for Repurposing of Personal Protective Masks *ACS Appl. Mater. Interfaces* **13** 12912–27

[37] Roy S, Mondal A, Yadav V, Sarkar A, Banerjee R, Sanpui P and Jaiswal A 2019 Mechanistic Insight into the Antibacterial Activity of Chitosan Exfoliated MoS2 Nanosheets: Membrane Damage, Metabolic Inactivation, and Oxidative Stress *ACS Appl. Bio Mater.* **2** 2738–55

[38] Sahoo D, Kumar B, Sinha J, Ghosh S, Roy S S and Kaviraj B 2020 Cost effective liquid phase exfoliation of MoS2 nanosheets and photocatalytic activity for wastewater treatment enforced by visible light *Sci. Reports 2020 101* **10** 1–12

[39] Hendricks N R, Watkins J J and Carter K R 2011 Formation of hierarchical silica nanochannels through nanoimprint lithography *J. Mater. Chem.* **21** 14213–8

[40] McIntyre N S, Spevack P A, Beamson G and Briggs D 1990 Effects of argon ion bombardment on basal plane and polycrystalline MoS2 *Surf. Sci.* **237** L390–7

[41] Durbin T D, Lince J R, Didziulis S V., Shuh D K and Yarmoff J A 1994 Soft X-ray photoelectron spectroscopy study of the interaction of Cr with MoS2(0001) *Surf. Sci.* **302** 314–28

[42] Benoist L, Gonbeau D, Pfister-Guillouzo G, Schmidt E, Meunier G and Levasseur A 1994 XPS analysis of lithium intercalation in thin films of molybdenum oxysulphides *Surf. Interface Anal.* **22** 206–10

[43] Laviron E 1979 General expression of the linear potential sweep voltammogram in the case of diffusionless electrochemical systems *J. Electroanal. Chem. Interfacial Electrochem.* **101** 19–28

[44] Khamlichi R El, Bouchta D, Anouar E H, Atia M Ben, Attar A, Choukairi M, Tazi S, Ihssane R, Faiza C, Khalid D and Khalid R T 2017 A novel l-leucine modified Sol-Gel-Carbon electrode for simultaneous electrochemical detection of homovanillic acid, dopamine and uric acid in neuroblastoma diagnosis *Mater. Sci. Eng. C* **71** 870–8

[45] Rose C, Parker A, Jefferson B and Cartmell E 2015 The characterization of feces and urine: A review of the literature to inform advanced treatment technology *Crit. Rev. Environ. Sci. Technol.* **45** 1827–79

[46] Bouatra S, Aziat F, Mandal R, Guo A C, Wilson M R, Knox C, Bjorndahl T C, Krishnamurthy R, Saleem F, Liu P, Dame Z T, Poelzer J, Huynh J, Yallou F S, Psychogios N, Dong E, Bogumil R, Roehring C and Wishart D S 2013 The Human Urine Metabolome *PLoS One* **8**

[47] Nikolac Gabaj N, Miler M, Unic A, Milevoj Kopcinovic L, Vrtaric A and Culej J 2020 Ascorbic acid in urine still compromises urinalysis results *Ann. Clin. Biochem.* **57** 64–8

[48] Huynh T P and Le T-A 2018 CHAPTER 2:Synthetic Chemistry for Molecular Imprinting *RSC Polym. Chem. Ser.* 28–64

[49] Makrlíkovμ A, Ktena E, Economou A, Ischer J, Navrμtil T, Barek J, Makrlíkovμ] A, Ischer J F, Barek J, Vyskočil V, Avrμtil T N, Heyrovsky´institute J, Heyrovsky´institute H, Ktena E and Economou A 2017 Voltammetric Determination

of Tumor Biomarkers for Neuroblastoma (Homovanillic Acid, Vanillylmandelic Acid, and 5-Hydroxyindole-3-acetic Acid) at Screen-printed Carbon Electrodes *Electroanalysis* **29** 146–53

[50] Libansky M, Zima J, Barek J and Dejmkova H 2016 Voltammetric determination of homovanillic acid and vanillylmandelic acid on a disposable electrochemical measuring cell system with integrated carbon composite film electrodes *Monatshefte fur Chemie* **147** 89–96

[51] Selvaraju T and Ramaraj R 2007 Simultaneous detection of ascorbic acid, uric acid and homovanillic acid at copper modified electrode *Electrochim. Acta* **52** 2998–3005